



# **Experimental and Numerical Investigation in Directed Energy Deposition for Component Repair**

Lan Li, Xinchang Zhang \* and Frank Liou



Department of Mechanical & Aerospace Engineering, Missouri University of Science and Technology, Rolla, MO 65401-0900, USA; ll752@mst.edu (L.L.); liou@mst.edu (F.L.)

\* Correspondence: xinchang.zhang@mst.edu

Abstract: Directed energy deposition (DED) has been widely used for component repair. In the repair process, the surface defects are machined to a groove or slot and then refilled. The sidewall inclination angle of the groove geometry has been recognized to have a considerable impact on the mechanical properties of repaired parts. The objective of this work was to investigate the feasibility of repairing various V-shaped defects with both experiments and modeling. At first, the repair volume was defined by scanning the defective zone. Then, the repair volume was sliced to generate the repair toolpath. After that, the DED process was used to deposit Ti6Al4V powder on the damaged plates with two different slot geometries. Mechanical properties of the repaired parts were evaluated by microstructure analysis and tensile test. Testing of the repaired parts showed excellent bonding between the deposits and base materials with the triangular slot repair. 3D finite element analysis (FEA) models based on sequentially coupled thermo-mechanical field analysis were developed to simulate the corresponding repair process. Thermal histories of the substrate on the repair sample were measured to calibrate the 3D coupled thermo-mechanical model. The temperature measurements showed very good verification with the predicted temperature results. After that, the validated model was used to predict the residual stresses and distortions in the parts. Predicted deformation and stress results can guide the evaluation of the repair quality.

Keywords: component repair; directed energy deposition; additive manufacturing; damage; deformation; residual stress

#### check for undates

Citation: Li, L.; Zhang, X.; Liou, F. Experimental and Numerical Investigation in Directed Energy Deposition for Component Repair. Materials 2021, 14, 1409. https:// doi.org/10.3390/ma14061409

Academic Editor: Irina Hussainova

Received: 19 February 2021 Accepted: 11 March 2021 Published: 14 March 2021

Publisher's Note: MDPI stays neutral with regard to jurisdictional claims in published maps and institutional affiliations.



Copyright: © 2021 by the authors. Licensee MDPI, Basel, Switzerland. This article is an open access article distributed under the terms and conditions of the Creative Commons Attribution (CC BY) license (https:// creativecommons.org/licenses/by/ 4.0/)

## 1. Introduction

Many metallic components are frequently subjected to severe working conditions during service, such as alternating heavy loads, high temperature, high pressure, and wear, which can easily cause defects on these parts. Frequent failures of these components can lead to a severe drop in productivity and process efficiency. Repair or remanufacturing damaged components provides solutions to increase their life economically with minimal interruption in the production process. The typical repair process mainly involves two steps. First, the irregular surface defects are machined by creating a V-shaped groove. Second, suitable materials are deposited back into the damaged zone using welding or additive manufacturing methods [1]. The laser-aided directed energy deposition (DED) process has shown great applications in the field of component repair [2,3]. DED is a typical additive manufacturing process that can create fully dense complex parts by directly melting materials and depositing them on the workpiece layer-by-layer following a user-defined tool path [4–7]. In this process, a high-power laser with a very small concentration area is used to create a molten pool on the damaged parts. The filler material, usually powders, experiences melting and cooling, and then solidifies to form the deposits. The deposits are usually fully dense and can form an excellent bond with the base parts [8,9] and have high mechanical properties, including tensile strength and fracture toughness [10,11]. For component repair, DED outperforms conventional repair approaches, with the following

Materials **2021**, 14, 1409 2 of 16

advantages: (1) precise control of the heating and deposition rate over the geometry and substrate; (2) better compatibility with many advanced materials; and (3) automation capability [12–16].

In the pre-repair process, a V-groove down to the defects is first obtained by removing the defects and surrounding materials so that the DED tools can access the damaged zone. After that, the repair volume is defined, and the damage is then refilled by depositing appropriate materials following the defined repair volume. In the DED process, a highenergy laser beam emits the powder nonuniformly. This high-intensity laser can produce complex thermal history and significant thermal residual stresses. Residual stress induced by a high thermal gradient is likely to cause distortion, cracking, and fatigue failure and impacts the quality of the repaired product. Many endeavors have been made to alleviate the undesirable effects and hence reduce the defects of the finished part. It has been recognized that V-groove geometry imposes a considerable impact on the mechanical performance of finished parts. For example, Graf [17] has analyzed the feasibility of laser metal deposition for refilling different V-groove shapes with both stainless steel and Ti6Al4V by experiments. They reported that the V-groove should be wide enough to ensure a successful rebuild without defects. Pinkerton [18] machined varied V-groove-shaped defects on H13 tool steel substrates and then repaired the missing volumes using the DED process. They concluded that a steep sidewall tilt angle cannot guarantee good metallurgical bonding between the as-deposited material and damaged parts because of the lower laser energy on the steep sidewall. Zhang et. al. [19] repaired three V-shaped defects with varied sidewall inclination angles on H13 tool steel substrates with a cobaltbased alloy. The microstructure and mechanical properties of rebuilt samples revealed that materials can be successfully deposited on H13 tool steel, except for 90° sidewall damage with a lack of fusion and many pores. Some works have tried to accomplish better repair performance under slot geometry with various materials [20–23]. Paul et. al. [24] reported that they were able to produce fully dense and crack-free WC-Co coatings on low carbon steel with excellent interfacial bonding and much higher hardness. Zhang et al. [25–27] repaired damaged compressor blades and damaged dies using the DED process. They concluded that the sidewall inclination angle of the slot should be carefully determined to obtain high-quality repair.

It is instructed that the sidewall tilt angle for V-groove geometry considerably affects the bonding condition of the filler material and substrate since it affects how laser melts the materials on the sidewall. However, there is no direct evidence to demonstrate the causality in the current literature. A clear understanding of that causality helps to optimize the sidewall inclination angle and hence produces good products. Therefore, it is of particular importance to elucidate the fusion conditions and temperature distribution with metallurgical bonding. Previous studies mainly focused on microstructure and performance testing analysis by experiments, finding that it is not easy to measure temperature evolution in the melt pool. In this study, the temperature and stress evolution in the DED process was tracked by both numerical and experimental analysis. With this information, the effect of sidewall inclination angle on the emergence of defects in repaired parts can be clearly understood. The thermal history and laser intensity in the DED process can also be analyzed in order to optimize design or geometry.

The objective of this paper was to investigate the influence of V-groove geometry sidewall angles on the properties of repaired parts through both experiments and numerical modeling. In the experimental part of the study, to perform the repair, V-shaped defects with different sidewall inclination angles were prepared on Ti6Al4V substrates. The repair volume on each substrate was reconstructed by scanning the damaged region using a 3D scanner. After this, the repair toolpath was generated. Then, Ti6Al4V powders were deposited on the damaged parts using the DED process. Subsequently, the repaired parts were tested by microstructure analysis and mechanical testing. In the modeling part of the study, 3D FEA models based on sequentially coupled thermo-mechanical field analysis were developed to simulate the repair process. The simulation accurately predicted

the study, 3D FEA models based on sequentially coupled thermo-mechanical field analysis were developed to simulate the repair process. The simulation accurately predicted temperature and residual stress on the repaired parts. The distortion and residual stress were evaluated to study the influence of the sidewall inclination angles on repair quality 16 Finally, conclusions were drawn for these two repair samples.

2. Experimental Procedure temperature and residual stress on the repaired parts. The distortion and residual stress 2.1. Material Preparation and Experimental Setup were evaluated to study the influence of the sidewall inclination angles on repair quality. Finall orden de professor formet bedrapair for blood by two tangular plates with dimensions of 60 mm × 19 mm ×10 mm were selected as the substrates. Two different slot geometries were maclain Experimental Procedura e triangular with a sidewall inclination angle of 45° (Figure 12) And Contract Evanguation with Experimental Contraction angle of 90° (Figure 1b). Ti6Al4V powders with particlesizes of the 159 my toxix vhosen gathest act with waterial of the chomical. campositiano notationed street is the track of the composition of the on the substrates: one triangular with a sidewall inclination angle of 45° (Figure 1a) and Table 1-Champical composition of the threat with particle sizes of 50–150 mm were chosen as the feedstock material. The chemical compositions of Ti6Al4V Ti6Al4V are listed in Table 1 [28] 4.5 0.25

6.76

0.2

Balance

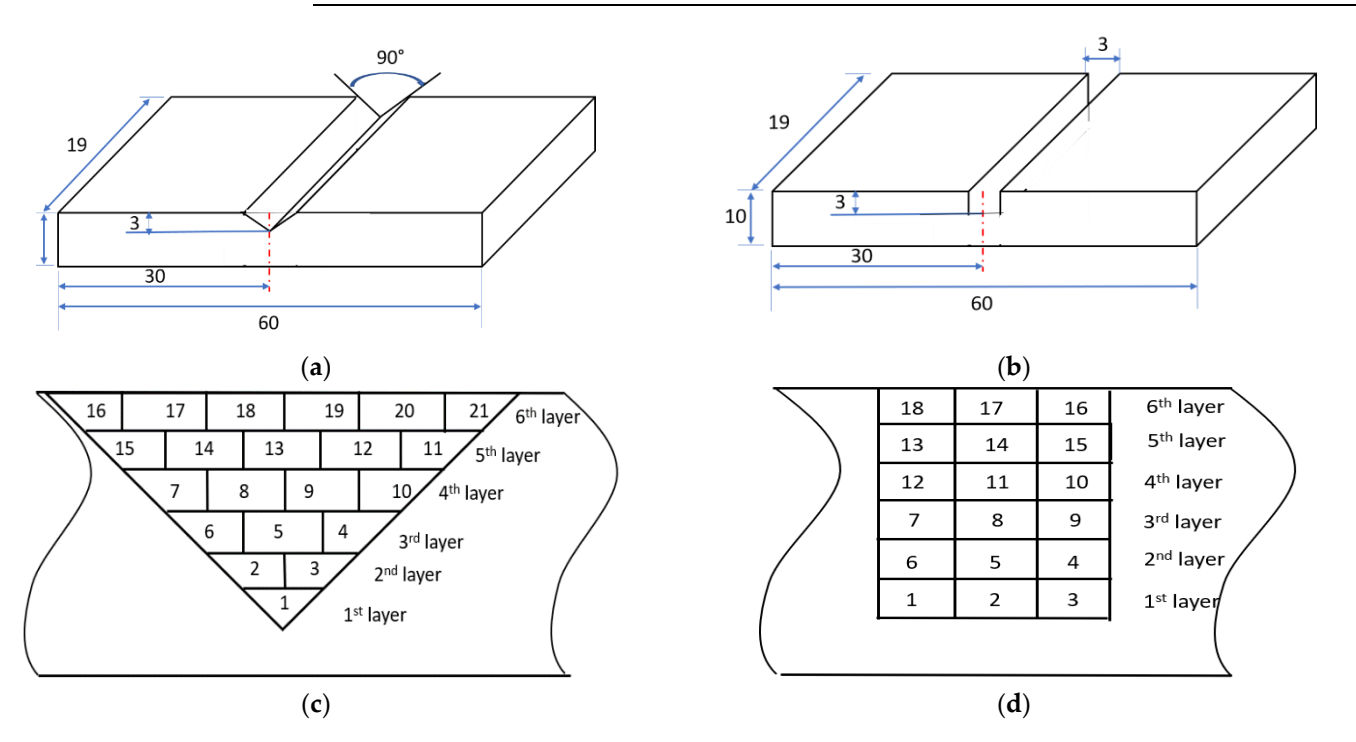


**Figure 1.** Schematic of the damaged substrates with triangular (a) and rectangular (b) slots; schematic of the scanning layers 1. Schematic of the damaged substrates with triangular (a) and rectangular (b) slots; schematic of the scanning layers layers and tracks in the damaged substrates with triangular (c) and rectangular (d) slots. and tracks in the damaged substrates with triangular (c) and rectangular (d) slots.

The missing volume on each substrate should be determined to obtain the tool path for material deposition. The deposition tool path directly determines the restored geometry pad has large effects on the quality of the repaired parts. In order to obtain the missing volume, the algorithm presented in [19] was used In this process, the missing volume was directly reobtained by scanning the defective area using a structure-light 3D scanner (O) timScan 5M, Shining 3D, San Francisco, CA, USA). After the missing volume was reconstructeth aneissing and was general substrates that driver mined to be this stage to almost wfor snaterial depositions. The damasition technost being the descriptions the destored secondary oand bestasse effects against interpretation of the control of the fivelymetithe algorithm prasente the laser was used. In this process the missing evolume trives directly replaced by scanning the defective area using a structure-light 3D scanner (OptimScan 5M, Shining 3D, San Francisco, CA, USA). After the missing volume was reconstructed, the tool path was generated based on the missing volume. The missing volume was sliced into 6 layers with a layer thickness of 0.5 mm. The tool path consists of an outline contour and a zigzag infill pattern, which indicates that the laser scans the outline first and then the zigzag pattern. The laser tracks for the two different damaged geometries are schematically shown in Figure 1c,d.

After the repair tool path was acquired, the damaged substrates were repaired using a Deters the repair tool stally, when priviled the damaged substrates mere repaired using a Deters the repair tool stally, when priviled the damaged substrates mere repaired using a Deters the repair tool stally, when Department of the damaged substrates mere repaired using the processing of the priviled powers for the damaged substrates are repaired to the repair tool path as a moved according to the repair tool path at the was processing parameters are listed in Table 2. In the experiment, the substrate was processing a parameters are preventing to the repair tool path at the was processing a parameter size in Table 3. In the experiment, the substrate was processing a parameter of preventing to be preventing to preventing to preventing to preventing the same levels of power, powder flowrate, and traverse speed were used in each experiment.

**Table 2.** Processing parameters for the repair experiment

lable 2. Processing parameters for the repair experime	III.
Experiment Parameters	Values
Experiment Parameters	Values/
Powderflow rate Powder flow rate Scan speed Scan speed Laser diameter Laser tidineters	295 by Main 218 5 mm/min 210 mm/min 1 mm (955 mm

## 2.2. Sa Sapur le reparation and Material Characterization

The has a sepond street and proceed with the same of t Ind., Rakanto, vit. I USAS A) edectricistins baran annahine (FIV). Anthen samples every staund ususing milition arthideaphrasive papers from 120 grit to 1200 grit in requence. Next the namsambses we redished the inside an and austrepsions of the property of the property and another sense and tinally firmalished switch with prousiling mispensions. After that, that polished specimen myspervets bed etanith Krall kratiseet. The maphology only aire tracture the energy was in the control of the c HIKEXKO-ETAB QXIREXKAMEREKENIK, NSA) SIRTISATING ANG ETAB QXIREXKAMEREKENIKA ANG ETAB 60(TITH renn Ei Fitsh Sc Buttidiut i Wallalman M. M. J. S. Scaning El Ettern del intercopo (S ESEMT) he Thententically boundary bot weem the refilled material and substrates was sutdicted AA nongraydispersive were represented to the property of the contract of antdyzzaelyzaneluni cotalpositioositiionsitiiotistoilbiintoilbu Tiensi [Fetastingesting on atvoord to teelt the est mebleamical principal times per this separation of the disparation of layers-whick day from cachute from edaulo sepatered ith bother twith or idhuationed an iFigure ted. in Theiguine 2 an Filers the citeresite were inectioned from the solitoned from start filers the citeresite were inectioned from the solitoned from t tem filhe preninterpreninterprinter die pfliqueter 2 Bigfanct 2 ter Bildes preninterpreninter bestehe beitsteand osits strades with rate in with an ion to ted cet the are it all that thick the coin the Thectensile Test was ile constructed using actellisting testen (Mindels 200) Moith a 3300 sheath a percention of the construction o Tensile stress strain survessment obtained obtained.

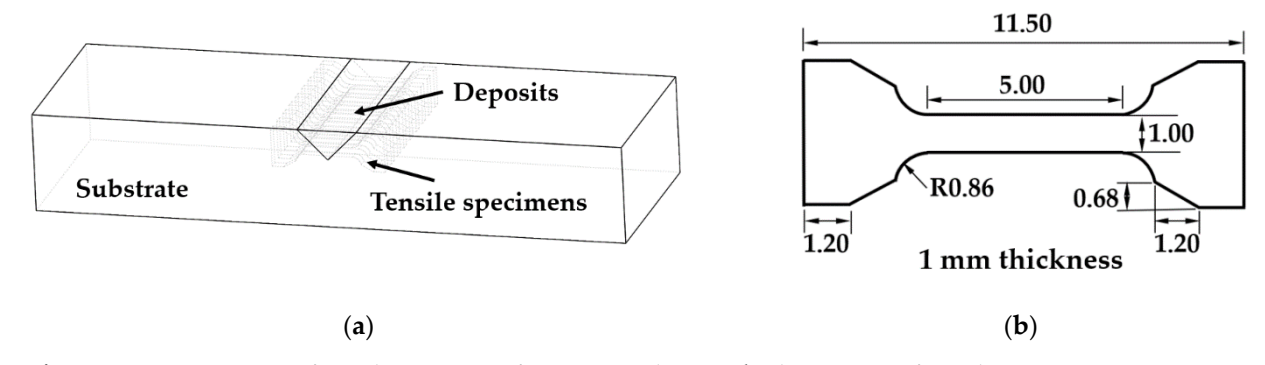


Figure 2. (a) Preparation of tensile specimens from repaired parts; (b) dimensions of tensile specimens (unit: mm). Figure 2. (a) Preparation of tensile specimens from repaired parts; (b) dimensions of tensile specimens (unit: mm).

# 2.3. Microstructure 2.3. Microstructure

Figure 3a,b reveal the images of the repaired parts with triangular and rectangular Figure 3a,b reveal the images of the repaired parts with triangular and rectangular defects, respectively. An overview of the cross-sections of the triangular and rectangular defects, respectively. An overview of the cross-sections of the triangular and rectangular

defects is shown in Figure 3c, d. respectively. It can be observed from Figure 3c, d. that the defects is shown in Figure 3c, d. respectively. It can be observed from Figure 3c, d. that the as deposited materials bonded well with the base part for the friangular case. However, as detections an interest of the rectangular defect case, very large pores were found near the edge of the wall for the rectangular defect case, very large pores were found near the edge of the wall for the rectangular defect case, very large pores were found near the edge of the wall of the rectangular defect as every large pore decease the sidewall due to its vertical is food as eccarity large pores were found access the sidewall due to its vertical is food as eccarity large pore defect the following microstructure analysis and tensity geometry. Because of this large pore defect, the following microstructure analysis and tensity geometry because of this large pore defect, the following microstructure analysis and tensity analyses were not performed within the rectangular repair plate. The repair plate tensingly severe most performed within the rectangular repair plate. The repaired plate tensingly severe most performed within the rectangular repair plate. The repaired for microstructure analysis in an analysis and with mangular defects was prepaired for microstructure analysis. The micrographs of the plates with the substrate analysis of the consistent of the deposits and the interface with the substrate are shown in Figure 4. Cross-sections of the deposits and the interface with the substrate are shown in Figure 5. In Figure 4 at Can be seen that the interface with the substrate are shown in Figure 5. In Figure 4 at Can be seen that the interface with the substrate are shown in Figure 5. In Figure 4 at Can be seen that the interface with the substrate are shown in Figure 5. In Figure 4 at Can be seen that the interface with the substrate of the defects at the figure 4 at Can be seen that the interface of the substrate of the continuou

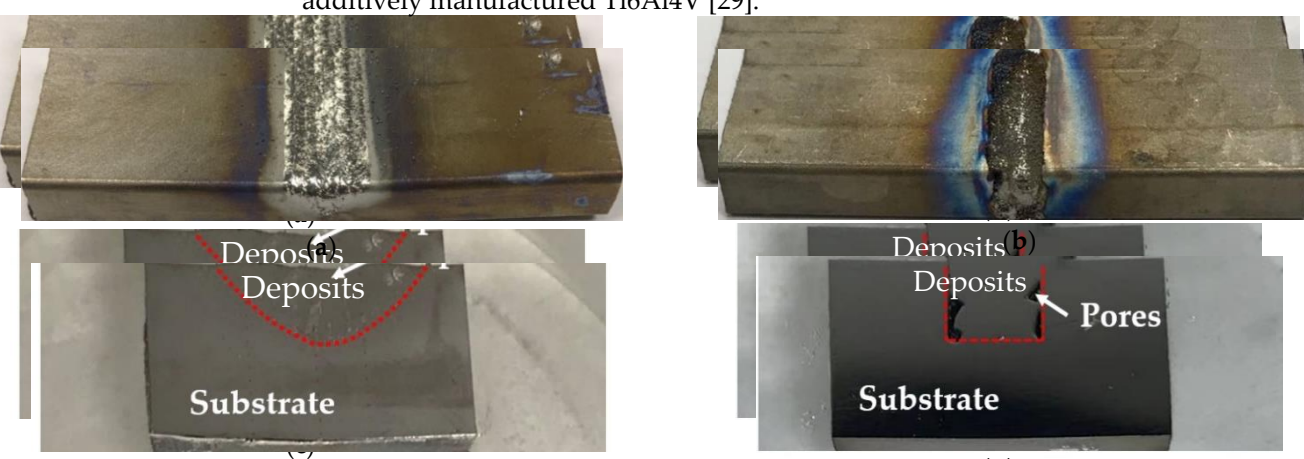


Figure 3. Repaired substrates with triangular (a) and rectangular (b) slots; overview of the cross-section of the repaired figure 3. Repaired substrates with triangular (a) and rectangular (b) slots; overview of the cross-section of the repaired substrates with triangular (c) and rectangular (d) slots (b) slots; overview of the cross-section of the repaired substrates with triangular (c) and rectangular (d) slots.

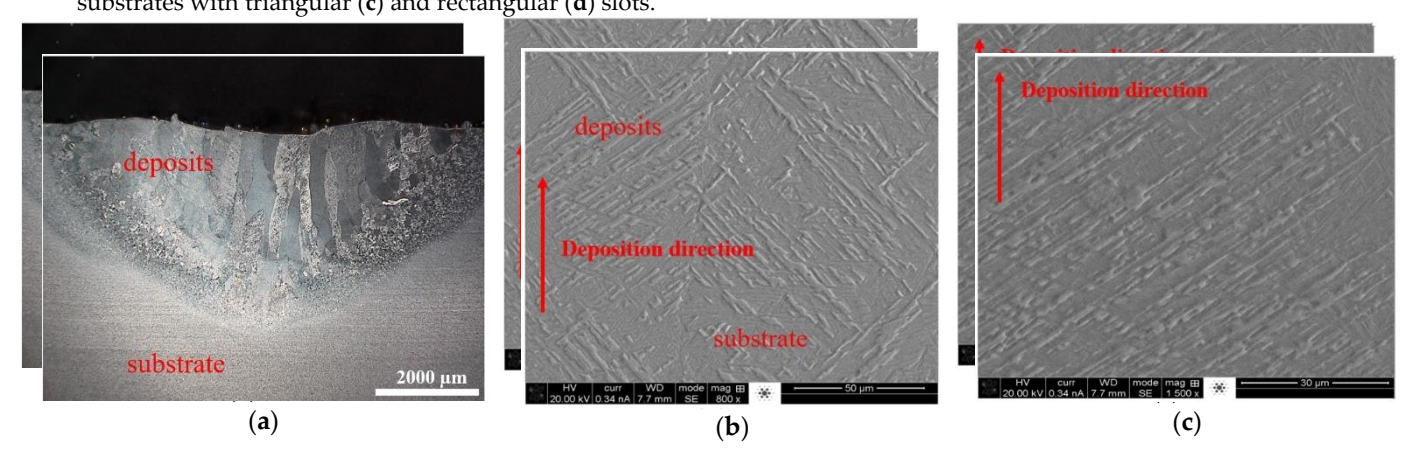


Figure 4. Cont.

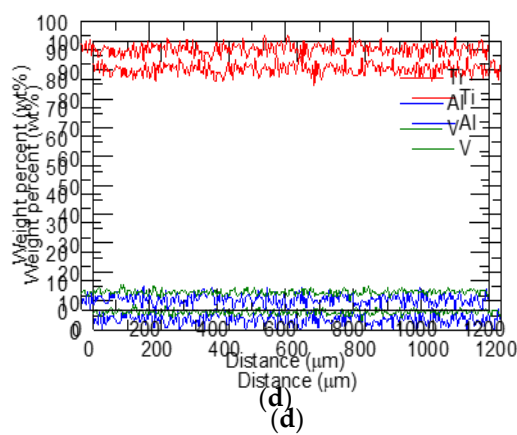


Figure 4. (a) Overview of the microstructure of the repaired region; (b) magnified view of the interface between deposits Figure 4. (a) Overview of the microstructure of the repaired region; (b) magnified view of the interface between deposits and substrate; and substrate; (c) microstructure of deposits; (d) elemental distribution over the interface. (c) microstructure of deposits; (d) elemental distribution over the interface.

EDS line scan analyses were performed across the interface for the triangular case and the result scan analyses were performed across the interface for the triangular case and the result scan analyses were performed across the interface for the triangular case and the result scan analyses were performed across the interface for the triangular case and the result scan analyses were performed across the interface for the triangular case and the result scan analyses were performed across the interface for the triangular case and the result scan analyses were performed across the interface for the triangular case and the result scan analyses were performed across the interface for the triangular case and the result scan analyses were performed across the interface for the triangular case and the result scan analyses were performed across the interface for the triangular case and the result scan across the interface for the triangular case and the result scan across the interface for the triangular case and the result scan across the result scan and the result is shown in Figure 14. The entire limiting dine stamped deproximately it? 120 mm t is identifiable there was no drop or tise in elemental composition over the intertage Additive manufacturing estateled in a woifer and distribution enfedements oscions other interface.

2.4. Tensile Behavior
2.4. Tensile Behavior tested to evaluate the bonding strength between the as-deposited material and the sub-Acceptes on tably a terrished strength spiritually between the as-deposited material and the sub-strate. A representative tensile stress strain curve is shown in Figure 3. The deciding the sub-ustrated tensile strength of all the specimens are summarized in Table 3. The testing and ultimate tensile strength and ultimate summarized in Table 3. The testing showed that the vield strength and ultimate tensile strength of the repaired parts were 954 showed that the vield strength and ultimate tensile strength of the repaired parts were 954 showed that the vield strength and ultimate tensile strength of the repaired parts were 954 showed that the vield strength and ultimate tensile strength of the repaired parts were 954 showed that the vield strength and ultimate tensile strength the pamples fractured at the 13.7 ± 15.7 ± 15.7 ± 15.7 ± 15.7 ± 15.7 ± 15.7 ± 15.7 ± 15.7 ± 15.7 ± 15.7 ± 15.7 ± 15.7 ± 15.7 ± 15.7 ± 15.7 ± 15.7 ± 15.7 ± 15.7 ± 15.7 ± 15.7 ± 15.7 ± 15.7 ± 15.7 ± 15.7 ± 15.7 ± 15.7 ± 15.7 ± 15.7 ± 15.7 ± 15.7 ± 15.7 ± 15.7 ± 15.7 ± 15.7 ± 15.7 ± 15.7 ± 15.7 ± 15.7 ± 15.7 ± 15.7 ± 15.7 ± 15.7 ± 15.7 ± 15.7 ± 15.7 ± 15.7 ± 15.7 ± 15.7 ± 15.7 ± 15.7 ± 15.7 ± 15.7 ± 15.7 ± 15.7 ± 15.7 ± 15.7 ± 15.7 ± 15.7 ± 15.7 ± 15.7 ± 15.7 ± 15.7 ± 15.7 ± 15.7 ± 15.7 ± 15.7 ± 15.7 ± 15.7 ± 15.7 ± 15.7 ± 15.7 ± 15.7 ± 15.7 ± 15.7 ± 15.7 ± 15.7 ± 15.7 ± 15.7 ± 15.7 ± 15.7 ± 15.7 ± 15.7 ± 15.7 ± 15.7 ± 15.7 ± 15.7 ± 15.7 ± 15.7 ± 15.7 ± 15.7 ± 15.7 ± 15.7 ± 15.7 ± 15.7 ± 15.7 ± 15.7 ± 15.7 ± 15.7 ± 15.7 ± 15.7 ± 15.7 ± 15.7 ± 15.7 ± 15.7 ± 15.7 ± 15.7 ± 15.7 ± 15.7 ± 15.7 ± 15.7 ± 15.7 ± 15.7 ± 15.7 ± 15.7 ± 15.7 ± 15.7 ± 15.7 ± 15.7 ± 15.7 ± 15.7 ± 15.7 ± 15.7 ± 15.7 ± 15.7 ± 15.7 ± 15.7 ± 15.7 ± 15.7 ± 15.7 ± 15.7 ± 15.7 ± 15.7 ± 15.7 ± 15.7 ± 15.7 ± 15.7 ± 15.7 ± 15.7 ± 15.7 ± 15.7 ± 15.7 ± 15.7 ± 15.7 ± 15.7 ± 15.7 ± 15.7 ± 15.7 ± 15.7 ± 15.7 ± 15.7 ± 15.7 ± 15.7 ± 15.7 ± 15.7 ± 15.7 ± 15.7 ± 15.7 ± 15.7 ± 15.7 ± 15.7 ± 15.7 ± 15.7 ± 1

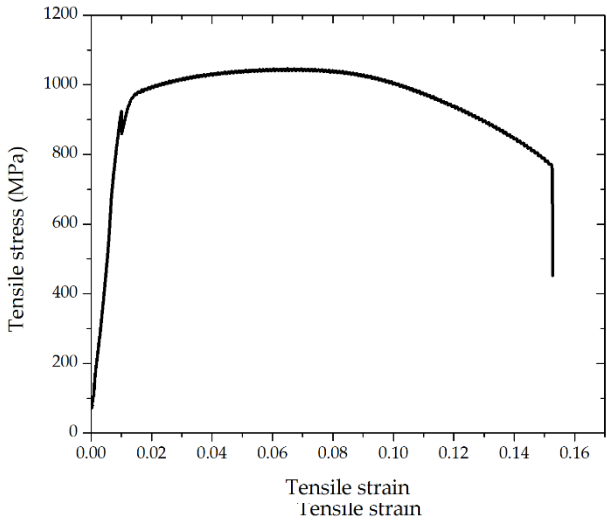


Figure 5. Tonsile stress-strain curve. Figure 5. Tensile stress-strain curve.

**Table 3.** Yield strength (YS) and ultimate tensile strength (UTS) of the repaired parts. **Table 3.** Yield strength (YS) and ultimate tensile strength (UTS) of the repaired parts

	V 5 1 1/1/2 1	
Sample #	13 (M1 a)	UIS (MII a)
Sample #	15 (1817a)	U15 (1911 a)
1	002.00 962.00	1046.32
$2^{1}$	10Pf x/2	106903 <del>~</del>
<del>-</del> 2	1011 82	1069 93
3	996.71	1058.80
3	<del></del>	1058.80
<u>~</u>		

Materials 2021, 14, 1409 7 of 16

**Table 3.** Yield strength (YS) and ultimate tensile strength (UTS) of the repaired parts. *Materials* **2021**, 14, x FOR PEER REVIEW

7 of 16
Sample # YS (MPa) UTS (MPa)

Sample #	YS (MPa)	UTS (MPa)
1	862.08	1046.32
	904:27	1869. <u>23</u> 1058.80 1078. <del>\$</del> 7
6	962.25	1034.4B
ø	994. <del>95</del> 7	<b>1028.43</b> 8
780899	93 <u>4</u> :77 95 <u>3</u> :25 978:30	1668.9 <u>8</u> 1606.12 1630.29
Average	954.49	1037.17
S.D.	<b>4</b> 7	<b>2</b> 1

## 3. Numerical Analysis of the Laser Repair Process

## 3.1. Model Setup

In the additive manufacturing process, due to the existence of rapid thermal cycles, residual stress and deformation inevitably occur. Numerical simulation is able to capture the temperature field and othermal tress a dielih in the pappirocess eshivitipo rates identifications lister to the properties of the propertie

First, the geometric model writh a striangal arace was as a stablished explanation street introduced was established for the established of strianger and the strianger of the s

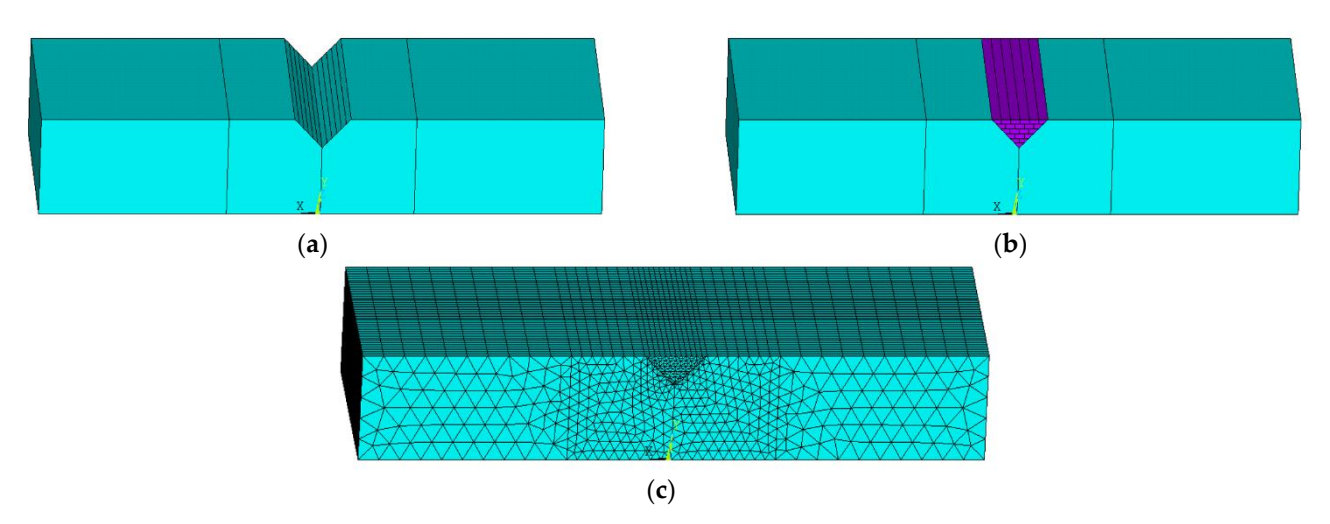


Figure 6: (a) FEA model geometry. Of the dampes of a party (b) Paser scarcen attractors for any dividing from the dampes of a party of the dampes of the dampes of a party of the dampes of a party of the dampes of the dampes of the dampes of a party of the dampes of the dampe

Table 4. Input parameters for the numerical simulation.

<b>Experimental Parameters</b>	Values
Power	650 W
Laser absorptivity	0.3

Materials **2021**, 14, 1409 8 of 16

<b>Experimental Parameters</b>	Values
Power	650 W
Laser absorptivity	0.3
Effective scan speed	210 mm/min
Laser diameter	1 mm
Time step	$0.1\mathrm{s}$

**Table 4.** Input parameters for the numerical simulation.

#### 3.2. Thermal and Mechanical Analysis

The transient temperature distribution in the entire volume of the material can be obtained from the 3D heat conduction equation [36]:

$$\frac{\partial(\rho c_p T)}{\partial t} = \frac{\partial}{\partial x} (k \frac{\partial T}{\partial x}) + \frac{\partial}{\partial y} (k \frac{\partial T}{\partial y}) + \frac{\partial}{\partial z} (k \frac{\partial T}{\partial z}) + Q \tag{1}$$

where k is the thermal conductivity;  $\rho$  is the density;  $c_p$  is the specific heat; all these thermal-mechanical properties are temperature-dependent; T is the current temperature; Q is the internal heat generation rate per unit volume; t is the time; and x, y, and z are the coordinates in the reference system.

The plate was clamped at the left and right surfaces. Both convection and radiation conditions were considered in all external surfaces, which were applied to all free surfaces. These heat transfer mechanisms are expressed as:

$$\ddot{q} = -k\frac{\partial T}{\partial z} + h(T - T_0) + \varepsilon\sigma\left(T^4 - T_0^4\right) \tag{2}$$

where T is the temperature of the workpiece, h is the heat transfer coefficient of natural convection, which is assumed to be dependent on temperature and is presented in Table 5,  $\sigma$  is the Stefan–Boltzmann constant of  $5.67 \times 10^{-8} \, \text{W/m}^2 \cdot \text{K}^4$  and  $\varepsilon$  is the surface emissivity of 0.3, and  $T_0$  is the ambient temperature, which is equal to the temperature at the initial time of 25 °C. Moreover, heat conduction at the contact interface between the plate and the clamping system is considered to account for the thermal inertia of the supporting structure. By correlating simulated and experimental results, the heat transfer coefficient used for Newton's model is set to 100 (W/m².°C).

**Table 5.** The convection heat transfer coefficient used in the simulation.

Temperature (°C)	25	200	400	600	800	1000	1500	2000
<i>h</i> (W/(m <sup>2</sup> ⋅K))	12	24	40	72	80	100	100	100

The stress equilibrium equation is written as [37,38]:

$$\nabla \cdot \sigma = 0 \tag{3}$$

where  $\sigma$  is the second-order stress tensor, associated with the material behavior law.

The total strain  $\varepsilon$  component, assuming small deformation thermo-elasto-plasticity, is represented as [39]:

$$\varepsilon = \varepsilon^e + \varepsilon^p + \varepsilon^{th} \tag{4}$$

where  $\varepsilon^e$ ,  $\varepsilon^p$ , and  $\varepsilon^{th}$  are the elastic strain, plastic strain, and thermal strain, respectively. The isotropic Hooke's law was used to model the elastic strain ( $\varepsilon^e$ ) in Equation (5). The thermal expansion coefficient was adopted to calculate the thermal strain in Equation (6). Elastic-plastic stain-stress behavior was described by a bilinear stress-strain curve starting at the origin, with positive stress and strain values, which was defined by the elastic

Materials **2021**, 14, 1409 9 of 16

modulus E, Poisson's ratio v, yield strength  $\sigma^Y$ , and tangent modulus G. This is called the bilinear isotropic hardening (BISO) model in ANSYS software.

The mechanical constitutive law can be written as [39]:

$$\sigma = C\varepsilon^{\ell} \tag{5}$$

where *C* is the fourth-order material stiffness tensor and  $\varepsilon^{e}$  is the second-order elastic strain tensor.

The thermal strain  $\varepsilon^{th}$  is given by [39]:

$$\varepsilon^{th} = \alpha \cdot \Delta T \tag{6}$$

where  $\alpha$  is the thermal expansion coefficient and  $\Delta T$  is the temperature change in a certain time duration.

#### 3.3. Heat Source Model and Material Properties

In temperature field analysis, the heat flux density load with uniform power density has been developed to model the heat input of the laser. The heat flux is applied to the active element of the powder via an ANSYS APDL subroutine. The heat source was considered a constant and uniformly distributed body heat flux, defined as:

$$Q = \frac{\alpha P}{\pi r^2 t} \tag{7}$$

where  $\alpha$  is the laser absorption coefficient, set as 0.3 according to the experiments, P is the power of the continuous laser, r is the radius of the laser beam, and t is the layer thickness.

The thermophysical properties and mechanical properties were temperature-dependent and identified in [35,40], as shown in Table 6.

Temperature (°C)	25	100	200	300	400	600	800	1200	1300	1600
Density, (kg/m <sup>3</sup> )	4420	4406	4395	4381	4366	4336	4309	4252	4240	3920
Thermal conductivity, (W/(mK))	7	7.45	8.75	10.15	11.35	4.2	17.8	23	24	50
Specific heat, (J/(kgK))	500	502	505	510	513	518	522	530	530	530
Thermal expansion coefficient, $(10^{-6}/K)$	10	10	10	10	10	10	10	11	11	11
Poisson's ratio	0.33	0.33	0.33	0.33	0.33	0.33	0.33	0.33	0.33	0.33
Elastic modulus, (GPa)	125	120	115	105	93	40	25	15	12	8
Yield strength, (MPa)	850	720	680	630	590	490	40	5	1	0.1

Table 6. Thermo-mechanical properties of the Ti6Al4V.

#### 4. Results and Discussion

### 4.1. Temperature Evaluation

Figure 7 presents the simulated temperature distribution at each deposition in the triangular defect case, where the laser is applied to the end of the 1st track in Figure 7a, followed by the 16th and 21st tracks in Figure 7b,c, respectively. The deposition of the first track generates a temperature of 1854 °C, and the substrate remains at a transient room temperature. Measured from the zoom-in temperature contours, the depth of the area where the temperature was higher than the melting point was 0.85 mm, as shown in Figure 7d (the zone encompassed by the grey color depicted in the melt pool). It can be observed that the melt depth was deep enough to enable fully metallurgical bonding between the first deposited layer and the base substrate. The deposition of the 16th and 21st tracks experienced temperatures of 2029 °C and 2284 °C, respectively, but higher temperatures

Materials **2021**, 14, 1409

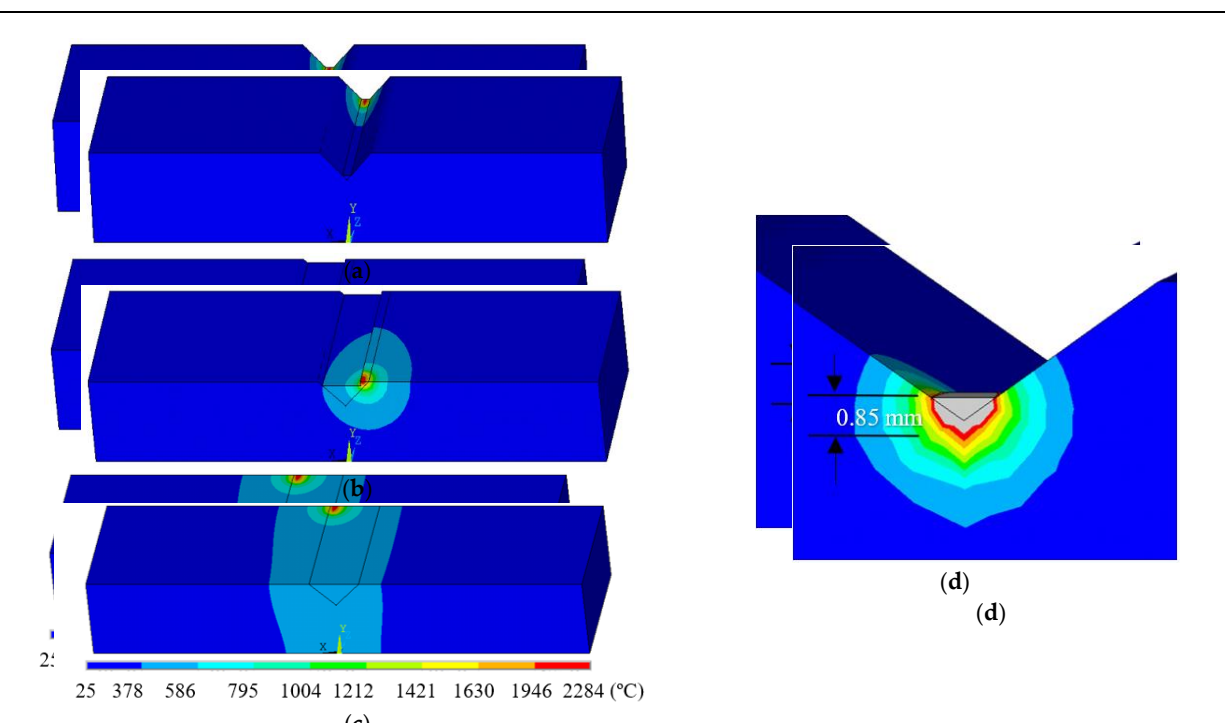


Figure 7. Temperature distribution at the end of the nth track, n is 1 (a), 16 (b), and 21 (c). The zoom-in temperature contours of the first track are shown in (d).

of the first track are shown in (d).

of the first track are shown in (d).

Figure 8b shows the simulated temperature history during the deposition process at Figure 8b shows the simulated temperature history during the deposition process at the selection process insular distribution of the selection process at the selection of the simulation of the selection of the sele

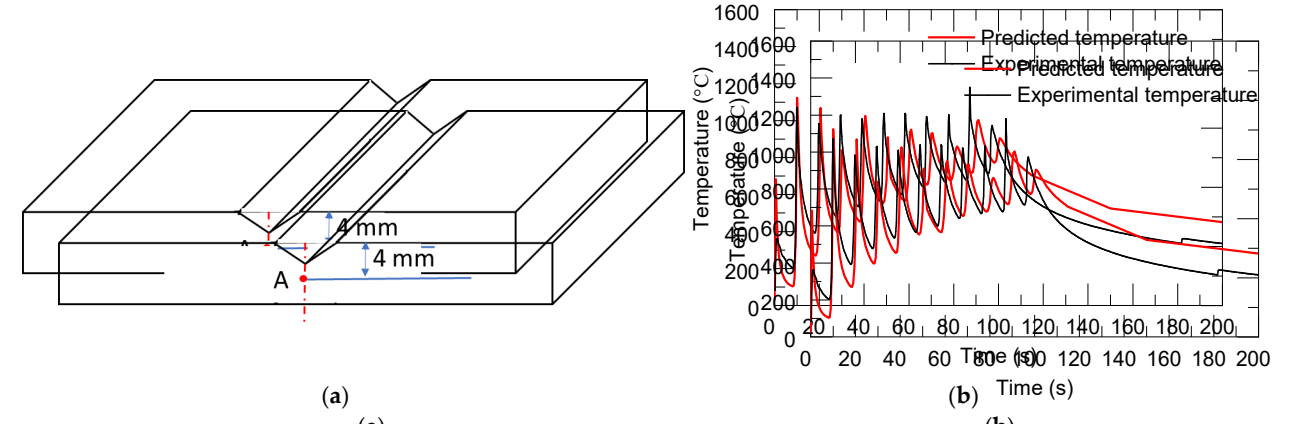


Figure 8. (a) The locations of each measurement, Point A (TC1); (b) the simulated and measured temperature history.

Figure 8. (a) The locations of each measurement. Point A (TC1); (b) the simulated and measured temperature history.

Figure 8. (a) The locations of each measurement, Point A (TC1); (b) the simulated and measured temperature history.

### 4.42 Disistentian and Stress Evaluation

Figure 9 shows the thermal access and distortion exallation in the longitudian direction of two selected points, 1 and 22, which made octand at the midd points of the first and ninth deposition tracks (shown in Figure 9a; point 1 lish in the substitute) BBth numerical covers above several peaks adve to the eggular movement of the disertless bource to deposit the different layers. As the laser hear source approaches the selected anni to the the mean and the made stars at this property the different layers. As the laser hear source approaches the selected anni to the the peat and the made stars at this property the different layers. As the laser hear source to the the temperature and the made stars are the deposition of the visit of point layers and the peat the selected and the temperature and the made stress was in the tensile state, with a value of 199 Mr a due to the material expansion by laser irritation. The deformation was relatively high because it was located at the bottom of the V-shaped groove. As the laser hear source moved, the temperature and thermal stress was in the tensile state, with a value of 199 Mr a due to the material expansion by laser irritation. The deformation was relatively high because it was located at the bottom of the V-shaped groove. As the laser hear source moved, the temperature and thermal stress kept changing. With the movement of the heat source to the upper layers and far away from point 1. The temperature and thermal stress also showed a decreasing trend. When a surface the deposition was completed, the accumulated heat gradually dissipated and the part gradually choice down. Material shrinkage was shown in the compressive state due to the cooling and shrinking of these deposited layers. This explains the longitudinal stress distributions (\$2) (along the laser moving direction) for different process times, shown in Figure 9c.

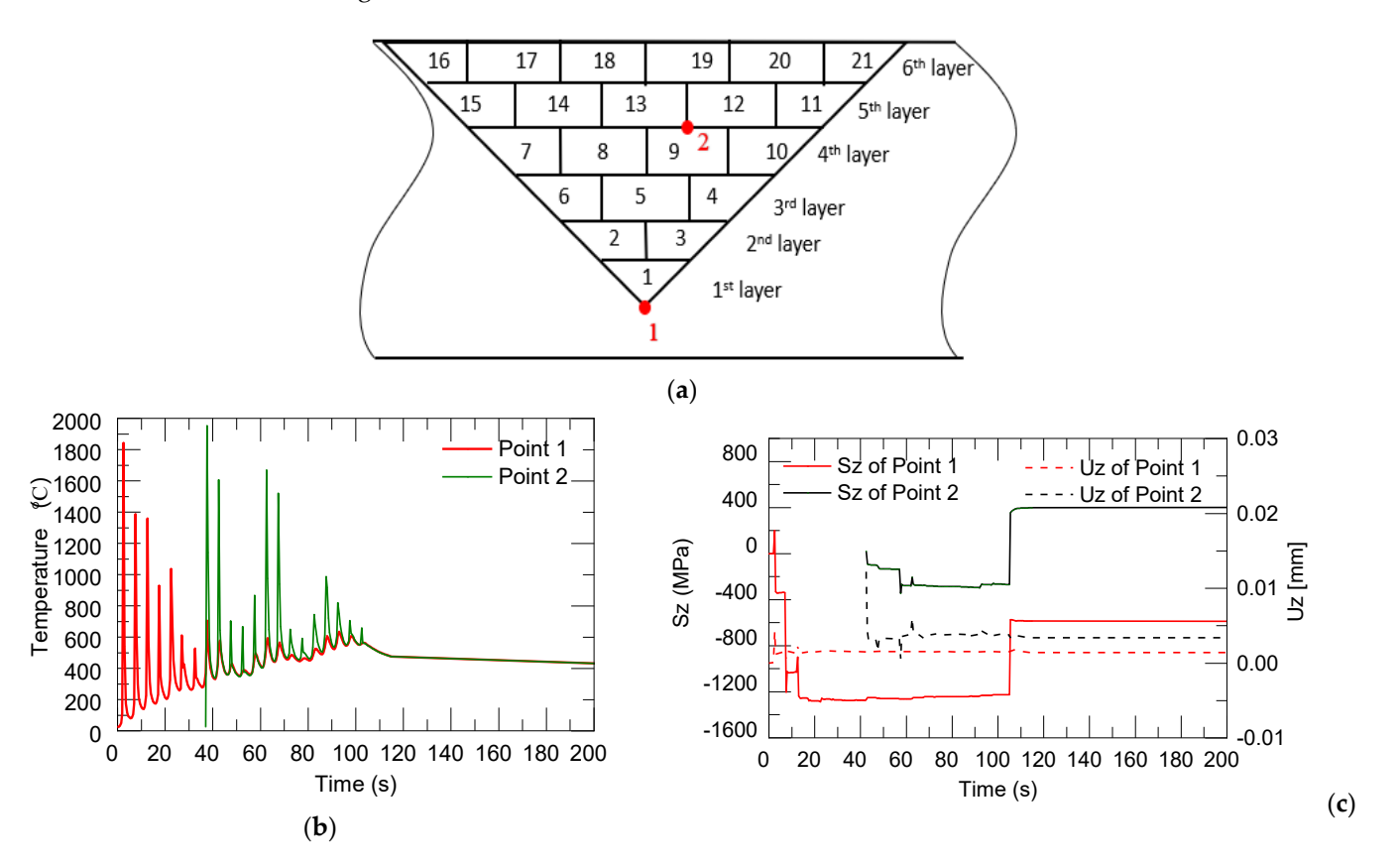


Figure 99. Less time of points I rank 2 (a). Curve agarding frequent temperature (b), the emalastress and distriction (2) on the first and night track.

Figure 10a snows threvaliational in the longitudinal istress after the first track. The thremate panish of the methodologic compression and the material pround this zone. Next, as the methodologic observed to the 8th makinthe quith layer (figure 10b), thre maximum compressions three source transferred and the hadret effective and (1442) below the methodologic observed to the large large to distinct the states are \$480 figure 10b). The continuous cooling to room

Materials 2021, 14, x FOR PEER REVIEW

12 of 16

1030 MPa were induced at the interface with the substrate. The continuous cooling to room temperature resulted in very high tensile stress values of 1525 MPa at the top surface of the substrate. resulted in very high tensile stress values of 1525 MPa at the top surface of the substrate.

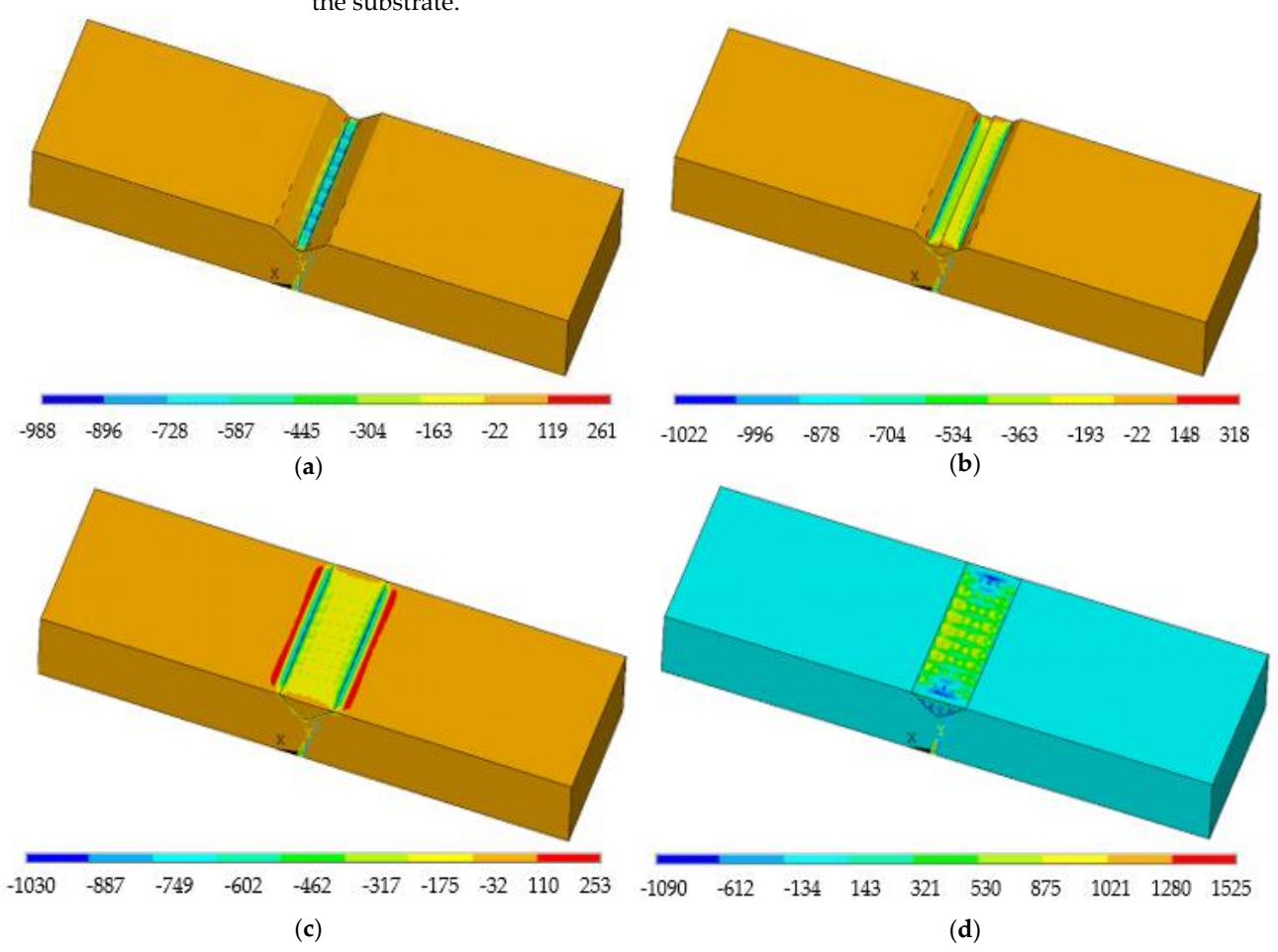


Figure 10.10 Congritudinal sites substribution at the end of the 1st (a), 4th (b), and final (c) tracks, and after cooling to moment temperature (d).

13 of 16

deposition was completed and after cooling to room temperature in the rectangular repair that extra stight it in increase that the theorem where the defect is deep and when the repair are is now the visit is stress that it is after cooling the close temperature in the triangular pentiture in the triangular and rectangular repair cases respectively. When referring to Lieft and Lright we observed and Lright we observed the same trend and magnitude level with each case in respect to the same trend and magnitude level with each case in respect to the von Mises stress distribution. As for the middle line, the von Mises stress values of the rectangular case (800–1000 MPa).

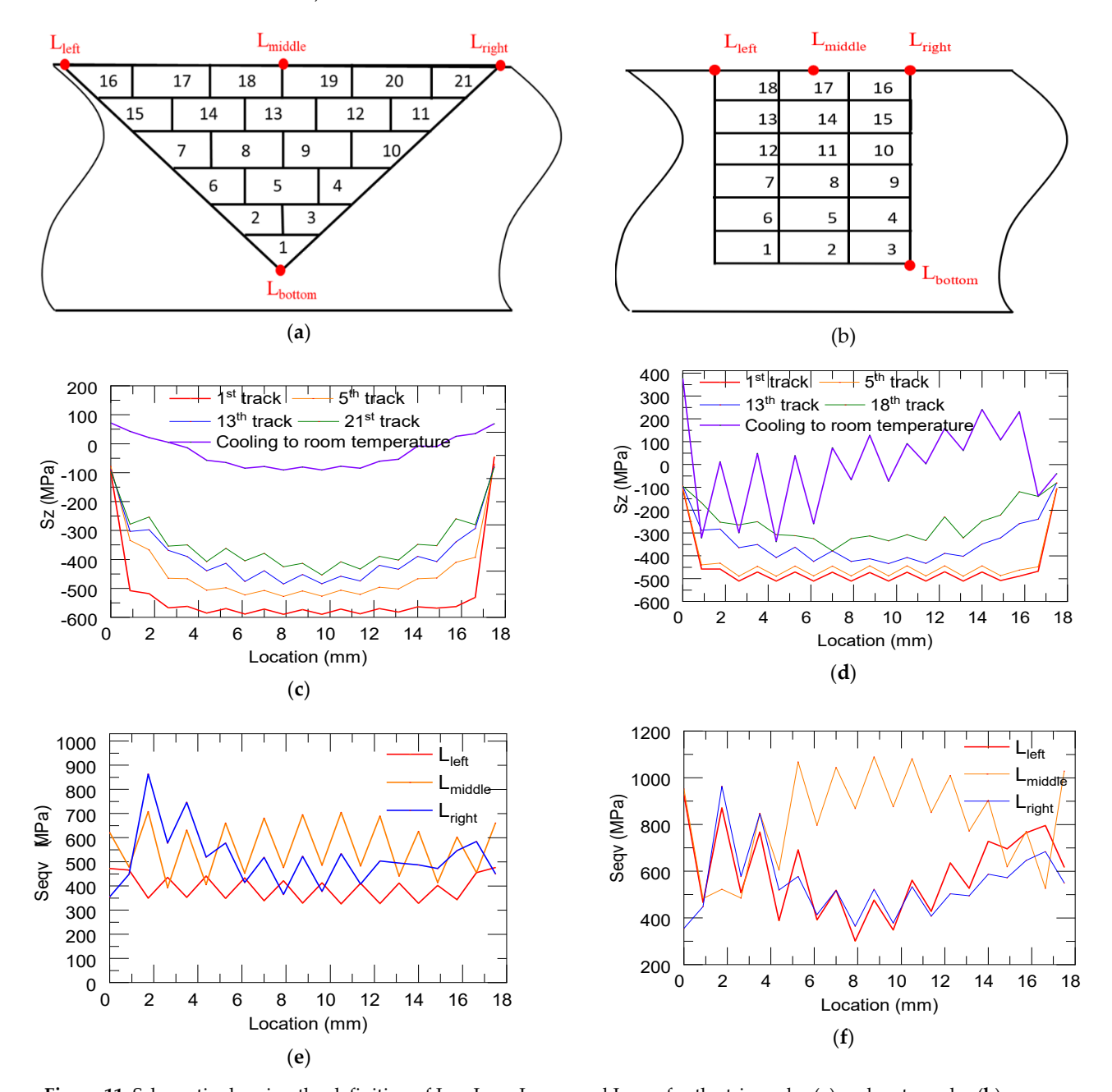
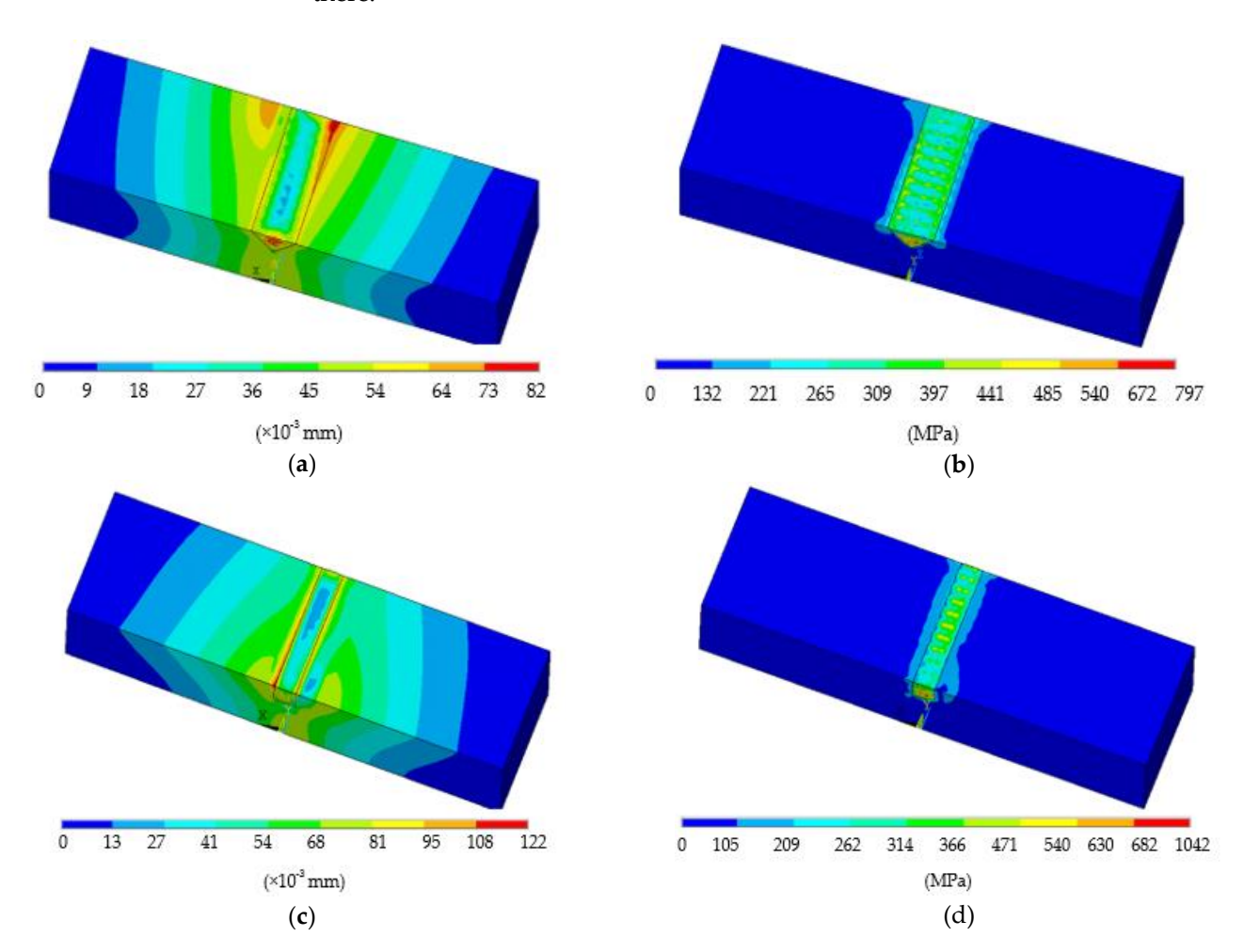


Figure 1.1 Schematic showing the definition of Left, L

The sum displacement and von Mises stress distribution after the deposition was completed and after cooling to room temperature in the triangular case are illustrated Materials **2021**, *14*, 1409

The sum displacement and von Mises stress distribution after the deposition was completed and after cooling to room temperature in the triangular case are illustrated in Figure 12a-b. The maximum displacement was formed at the interface region of the build-in-right of the Thamasimum displacement was formed at the interface region of the build-in-right of the Thamasimum displacement was formed at the interface region of the build-in-right of the Thamasimum displacement was formed at the interface region of the build-in-right of the Thamasimum displacement was formed at the interface region of the build-in-right of the Damasimum displacement was formed at the interface region of the build-in-right of the Damasimum displacement was formed at the interface region of the build-in-right of the Damasimum displacement was formed at the interface region of the Damasimum displacement disp



Figiture 17a (1) Spiralement vectorial, no. Usi, no. (Vo.) Von Miserest, escape are a deposition and ingolous on remptementa-in through this popular (e) cases.

## 5. Conclusions

In this study, we have presented a damage reconstruction method for V-shaped groove repairs using the directed energy deposition DED) process. The damaged parts had triangular or rectangular defects in cross-section. In this work, we investigated the feasibility of repairing two V-shaped defects with both experiments and modeling or he main conclusions are indicated below.

Ti6Al4V powder particles were deposited on the damaged region using the DED technique, following the repair toolpath. The microstructure analysis and tensile testing

Materials **2021**, 14, 1409 15 of 16

confirmed solid bonding along the interface for the triangular defect repair case. The tensile test showed an average ultimate tensile strength of 1037 MPa for the repaired parts, and samples fractured at the region of the deposits, not at the interface. However, for repairing the sample with rectangular damage, the filler material did not bond well with the substrate, causing a large number of pores.

3D finite element models based on sequentially coupled thermo-mechanical field analysis were developed to simulate the corresponding repair deposition processes. Finally, the average equivalent stresses and deformation in the triangular repair case showed low values at the intersection between the base plate and the deposited tracks than those in the rectangular repair case. The high equivalent stresses near the bottom deposition may induce cracks or delamination in the rectangular repair case. The predicted deformation and stress results will guide the evaluation of the quality of repaired parts based on repair slot geometry.

**Author Contributions:** Conceptualization, L.L., F.L. and X.Z.; methodology, L.L. and X.Z.; software, L.L.; validation, L.L. and X.Z.; investigation, L.L. and X.Z.; writing—original draft preparation, L.L.; writing—review and editing, X.Z.; supervision, F.L.; project administration, F.L.; funding acquisition, F.L. All authors have read and agreed to the published version of the manuscript.

**Funding:** This research was funded by National Science Foundation Grants, grant number CMMI 1625736.

**Institutional Review Board Statement:** Not applicable.

Informed Consent Statement: Not applicable.

**Data Availability Statement:** The data presented in this study are available on request from the corresponding author.

**Acknowledgments:** This research was supported by the Intelligent Systems Center, Center for Aerospace Manufacturing Technologies, and Material Research Center at Missouri S&T. Their financial support is greatly appreciated.

Conflicts of Interest: The authors declare no conflict of interest.

#### References

- 1. Zhang, X.; Cui, W.; Li, W.; Liou, F. A hybrid process integrating reverse engineering, pre-repair processing, additive manufacturing, and material testing for component remanufacturing. *Materials* **2019**, *12*, 1961. [CrossRef]
- 2. Nowotny, S.; Scharek, S.; Beyer, E.; Richter, K.-H. Laser beam build-up welding: Precision in repair, surface cladding, and direct 3D metal deposition. *J. Therm. Spray Technol.* **2007**, *16*, 344–348. [CrossRef]
- 3. Song, J.; Deng, Q.; Chen, C.; Hu, D.; Li, Y. Rebuilding of metal components with laser cladding forming. *Appl. Surf. Sci.* **2006**, 252, 7934–7940. [CrossRef]
- 4. Li, W.; Chen, X.; Yan, L.; Zhang, J.; Zhang, X.; Liou, F. Additive manufacturing of a new Fe-Cr-Ni alloy with gradually changing compositions with elemental powder mixes and thermodynamic calculation. *Int. J. Adv. Manuf. Technol.* **2018**, 95, 1013–1023. [CrossRef]
- 5. Zhang, K.; Liu, W.; Shang, X. Research on the processing experiments of laser metal deposition shaping. *Opt. Laser Technol.* **2007**, 39, 549–557. [CrossRef]
- 6. Mançanares, C.G.; de Zancul, S.E.; da Silva, C.J.; Cauchick, M.P.A. Additive manufacturing process selection based on parts' selection criteria. *Int. J. Adv. Manuf. Technol.* **2015**, *80*, 1007–1014. [CrossRef]
- 7. Vaezi, M.; Seitz, H.; Yang, S. A review on 3D micro-additive manufacturing technologies. *Int. J. Adv. Manuf. Technol.* **2013**, 67, 1721–1754. [CrossRef]
- 8. Rafi, H.K.; Starr, T.L.; Stucker, B.E. A comparison of the tensile, fatigue, and fracture behavior of Ti-6Al-4V and 15-5 PH stainless steel parts made by selective laser melting. *Int. J. Adv. Manuf. Technol.* **2013**, *69*, 1299–1309. [CrossRef]
- 9. Al-Jamal, O.M.; Hinduja, S.; Li, L. Characteristics of the bond in Cu-H13 tool steel parts fabricated using SLM. *CIRP Ann.* **2008**, 57, 239–242. [CrossRef]
- 10. Li, T.; Chen, Y.; Wang, L. Enhanced fracture toughness in architected interpenetrating phase composites by 3D printing. *Compos. Sci. Technol.* **2018**, *167*, 251–259. [CrossRef]
- 11. Khosravani, M.R.; Zolfagharian, A. Fracture and load-carrying capacity of 3D-printed cracked components. *Extrem. Mech. Lett.* **2020**, *37*, 100692. [CrossRef]
- 12. Borrego, L.P.; Pires, J.T.B.; Costa, J.M.; Ferreira, J.M. Fatigue behaviour of laser repairing welded joints. *Eng. Fail. Anal.* **2007**, 14, 1586–1593. [CrossRef]

Materials **2021**, 14, 1409 16 of 16

13. Zhong, M.; Liu, W.; Ning, G.; Yang, L.; Chen, Y. Laser direct manufacturing of tungsten nickel collimation component. *J. Mater. Process. Technol.* **2004**, *147*, 167–173. [CrossRef]

- 14. Borrego, L.P.; Pires, J.T.B.; Costa, J.M.; Ferreira, J.M. Mould steels repaired by laser welding. *Eng. Fail. Anal.* **2009**, *16*, 596–607. [CrossRef]
- 15. Wang, W.; Pinkerton, A.J.; Wee, L.M.; Li, L. Component repair using laser direct metal deposition BT. In Proceedings of the 35th International MATADOR Conference, Taipei, Taiwan, 27 July 2007; Hinduja, S., Fan, K.-C., Eds.; Springer London: London, UK, 2007; pp. 345–350.
- 16. Nikam, S.H.; Jain, N.K. Laser-based repair of damaged dies, molds, and gears BT. In *Advanced Manufacturing Technologies: Modern Machining, Advanced Joining, Sustainable Manufacturing*; Gupta, K., Ed.; Springer International Publishing: Cham, Switzerland, 2017; pp. 137–159. ISBN 978-3-319-56099-1.
- 17. Graf, B.; Gumenyuk, A.; Rethmeier, M. Laser metal deposition as repair technology for stainless steel and titanium alloys. *Phys. Procedia* **2012**, *39*, 376–381. [CrossRef]
- 18. Pinkerton, A.J. Advances in the modeling of laser direct metal deposition. J. Laser Appl. 2014, 27, S15001. [CrossRef]
- 19. Zhang, X.; Pan, T.; Li, W.; Liou, F. Experimental characterization of a direct metal deposited cobalt-based alloy on tool steel for component repair. *JOM* **2019**, *71*, 946–955. [CrossRef]
- 20. Renwei, L.; Zhiyuan, W.; Todd, S.; Frank, L.; Cedo, N. Stereo vision-based repair of metallic components. *Rapid Prototyp. J.* **2017**, 23, 65–73. [CrossRef]
- 21. Paydas, H.; Mertens, A.; Carrus, R.; Lecomte-Beckers, J.; Tchuindjang, J.T. Laser cladding as repair technology for Ti-6Al-4V alloy: Influence of building strategy on microstructure and hardness. *Mater. Des.* **2015**, *85*, 497–510. [CrossRef]
- 22. Mudge, R.P.; Wald, N.R. Laser engineered net shaping advances additive manufacturing and repair. Weld. J. 2007, 86, 44.
- 23. Song, L.; Zeng, G.; Xiao, H.; Xiao, X.; Li, S. Repair of 304 stainless steel by laser cladding with 316 L stainless steel powders followed by laser surface alloying with WC powders. *J. Manuf. Process.* **2016**, 24, 116–124. [CrossRef]
- 24. Paul, C.P.; Alemohammad, H.; Toyserkani, E.; Khajepour, A.; Corbin, S. Cladding of WC-12 Co on low carbon steel using a pulsed Nd:YAG laser. *Mater. Sci. Eng. A* **2007**, *464*, 170–176. [CrossRef]
- 25. Zhang, X.; Li, W.; Adkison, K.M.; Liou, F. Damage reconstruction from tri-dexel data for laser-aided repairing of metallic components. *Int. J. Adv. Manuf. Technol.* **2018**, *96*, 1–14. [CrossRef]
- 26. Zhang, X.; Li, W.; Chen, X.; Cui, W.; Liou, F. Evaluation of component repair using direct metal deposition from scanned data. *Int. J. Adv. Manuf. Technol.* **2018**, *95*, 3335–3348. [CrossRef]
- 27. Zhang, X.; Li, W.; Liou, F. Damage detection and reconstruction algorithm in repairing compressor blade by direct metal deposition. *Int. J. Adv. Manuf. Technol.* **2018**, *95*, 2393–2404. [CrossRef]
- 28. Li, W.; Liou, F.; Newkirk, J.; Taminger, K.M.B.; Seufzer, W.J. Investigation on Ti6Al4V-V-Cr-Fe-SS316 multi-layers metallic structure fabricated by laser 3D printing. *Sci. Rep.* **2017**, *7*, 7977. [CrossRef] [PubMed]
- Mills, K.C. Recommended Values of Thermophysical Properties for Selected Commercial Alloys; Woodhead Publishing: Cambridge, UK, 2002; ISBN 1855735695.
- 30. Farahmand, P.; Kovacevic, R. An experimental-numerical investigation of heat distribution and stress field in single- and multi-track laser cladding by a high-power direct diode laser. *Opt. Laser Technol.* **2014**, *63*, 154–168. [CrossRef]
- 31. Li, Q.; Gnanasekaran, B.; Fu, Y.; Liu, G.R. Prediction of thermal residual stress and microstructure in direct laser metal deposition via a coupled finite element and multiphase field framework. *JOM* **2020**, 72, 496–508. [CrossRef]
- 32. Mukherjee, T.; Zuback, J.S.; Zhang, W.; DebRoy, T. Residual stresses and distortion in additively manufactured compositionally graded and dissimilar joints. *Comput. Mater. Sci.* **2018**, *143*, 325–337. [CrossRef]
- 33. Yang, Q.; Zhang, P.; Cheng, L.; Min, Z.; Chyu, M.; To, A.C. Finite element modeling and validation of thermomechanical behavior of Ti-6Al-4V in directed energy deposition additive manufacturing. *Addit. Manuf.* **2016**, *12*, 169–177. [CrossRef]
- 34. Li, L.; Zhang, X.; Cui, W.; Liou, F.; Deng, W.; Li, W. Temperature and residual stress distribution of FGM parts by DED process: Modeling and experimental validation. *Int. J. Adv. Manuf. Technol.* **2020**, *109*, 451–462. [CrossRef]
- 35. Li, L.; Tan, P.; Xinchang, Z.; Yitao, C.; Wenyuan, C.; Lei, Y.; Liou, F. Deformations and stresses prediction of cantilever structures fabricated by selective laser melting process. *Rapid Prototyp. J.* **2021**, 39, 464–470.
- 36. Incropera, F.P.; DeWitt, D.P.; Bergman, T.L.; Lavine, A.S. Introduction to Heat Transfer; John Wiley & Sons: Hoboken, NJ, USA, 2006.
- 37. Megahed, M.; Mindt, H.-W.; N'Dri, N.; Duan, H.; Desmaison, O. Metal additive-manufacturing process and residual stress modeling. *Integr. Mater. Manuf. Innov.* **2016**, *5*, 61–93. [CrossRef]
- 38. Peyre, P.; Aubry, P.; Fabbro, R.; Neveu, R.; Longuet, A. Analytical and numerical modelling of the direct metal deposition laser process. *J. Phys. D. Appl. Phys.* **2008**, *41*, 25403. [CrossRef]
- 39. Irwin, J.; Michaleris, P. A line heat input model for additive manufacturing. J. Manuf. Sci. Eng. 2016, 138, 33662. [CrossRef]
- Lu, X.; Lin, X.; Chiumenti, M.; Cervera, M.; Hu, Y.; Ji, X.; Ma, L.; Yang, H.; Huang, W. Residual stress and distortion of rectangular and S-shaped Ti-6Al-4V parts by Directed Energy Deposition: Modelling and experimental calibration. *Addit. Manuf.* 2019, 26, 166–179. [CrossRef]